Continuous Growth of Germanene and Stanene Lateral Heterostructures

Tsuyoshi Ogikubo, Hiroki Shimazu, Yuya Fujii, Koichi Ito, Akio Ohta, Masaaki Araidai, Masashi Kurosawa, Guy Le Lay, Junji Yuhara

Continuous Growth of Germanene and Stanene Lateral Heterostructures

Tsuyoshi Ogikubo, Hiroki Shimazu, Yuya Fujii, Koichi Ito, Akio Ohta, Masaaki Araidai, Masashi Kurosawa, Guy Le Lay, and Junji Yuhara

Abstract

Group 14 elemental post-graphene materials receive much attention because of their outstanding properties, typically, as robust 2D topological insulators. Their heterostructures are a main target in view of disruptive applications. Here, the realization of striking in-plane lateral heterostructures between germanene and stanene are shown, which are sustainable 2D Ge- and Snbased graphene analogs, but with a strong intrinsic spin–orbit coupling. A unique combination of atomic segregation epitaxy (ASE) and molecular beam epitaxy (MBE) for the in situ continuous fabrication of nearly atomically precise lateral multijunction heterostructures, respectively, consisting of atom-thin germanene and stanene on a Ag(111) thin film is used. Scanning tunneling microscopy (STM) observations at atomic scale and low-energy electron diffraction

testify that germanene and stanene sheets without intermixing are prepared simultaneously on the same terraces at wide scale: tin and germanium atoms neither exchange their sites nor adsorb on the germanene and stanene sheets. The atomic structure of the boundary between germanene and stanene

is derived from STM images, while scanning tunneling spectroscopy reveals key electronic features at the heterojunction. This innovative synergetic approach of ASE and MBE growths offers great flexibility for the realization of unprecedented lateral 2D heterostructures.

1. Introduction

Group 14 elemental 2D materials with honeycomb struc- ture beyond graphene have attracted considerable interest recently. At variance with graphene, for which the opening of a band gap in its electronic structure is difficult, these novel 2D materials are expected to possess sizeable band gaps, making them typically suitable for elec- tronic applications. Furthermore, theory predicts that they are robust topological insulators, even up to about room tem- perature (RT) and above for germanene and stanene.

In experiment, these artificial 2D materials were firstly realized in situ by molecular beam epitaxy (MBE) for silicene in 2012,[1,2] germanene in 2014,[3] stanene in 2015,[4] and finally plumbene in 2019.[5] One of the next targets is the growth of in-plane heterostructures because abrupt lateral interfaces promise controlled heterojunction functionali- ties. Lateral heterostructures of graphene and hexagonal boron nitride (h-BN) were grown on Cu(110) in 2014.[6] First-princi- ples calculations on the electronic proper- ties of graphene quantum dots embedded in monolayer h-BN sheets typically indi- cate that the h-BN band gap shrinks upon

increasing the diameter of the graphene dots.[7] Besides lat- eral graphene/h-BN heterostructures, fabrication of several in-plane heterostructures of transition metal dichalcogenides has also been reported.[8] Very recently, vertical heterostruc- tures have been

prepared by boron intercalation underneath graphene, while, more strikingly, lateral integration of boro- phene with graphene has been realized.[9] At variance, there is no experimental report of the realization of such monolayer in-plane heterostructures for the group 14 post-graphene 2D materials, although each of them typically possesses very high hole and electron mobilities.[10] As stressed in Ref. [9], compared to vertical junctions with essentially van der Waals bonding, generally fabricated by mechanical stacking, 2D lat- eral heterostructures with covalent lateral stitching require bottom-up synthesis, which explains why such realizations are rare. However, the covalent in-plane bonding of lateral heterointerfaces for imperfect lattice matching often results in wide interfaces, where disorder and intermixing can reduce the structural and electronic abruptness. As a consequence, finding appropriate 2D materials and identifying synthetic conditions that yield nearly atomically sharp heterostructures is of major interest.

The energy gaps for silicene, germanene, and stanene are not so large, ranging from 0.002 to 0.03, and 0.1 eV, respectively.[11] Yet, 2D pseudomorphic heterostructures, for example, of silicene and germanene ribbons, might be used to control the electronic band structures, because the band gaps are made tunable by adjusting the widths of the respective nanoribbons.[12,13] Nevertheless, the realization of post-graphene lateral heterostructures based on group 14 elements, which is crucial for the future fabrication of heterojunction-embedded 2D devices compatible with conventional Si-based technology, remains a daunting challenge.

Silicene has been initially synthesized in situ on Ag(111), ZrB_2(0001), and Ir(111)[1,2,14] Next, the growth of germanene by MBE has been reported on Au(111),[3] Pt(111),[15] Al(111),[16] Sb(111),[17] Cu(111),[18] Ag(111),[19] Ge(110),[20] MoS_2,[21] graphite,[22] and Ge(111).[23] Recently, germanene has been also prepared on Ag(111) thin films by atomic segregation epitaxy (ASE).[24] For the MBE growth of stanene, Bi_2Te_3(111),[4] Sb(111),[25] Ag(111),[26] and Cu(111)[27] substrates have been adopted. Up to now, the Ag(111) surface appears as the most promising template for the heterostructure growth of all group 14 post-graphene materials. According to the phase diagram, Ge and Sn are immiscible at any ratio,[28] while Ge and Si can make all proportional solid solutions.[29] Therefore, germanene and stanene appear as a promising combination for realizing a lateral heterostructure on Ag(111).

In this work, we achieved lateral in-plane heterostructures of monolayer germanene and stanene on a silver (111) thin film epitaxially grown on a Ge(111) substrate, as shown in **Figure 1**. With a synergetic combination of in situ ASE for germanene and MBE for stanene, we found the appropriate kinetic conditions to realize simultaneously their lateral growths. Typically, after initial annealing of the sample at 500 °C, during slow cooling Ge segregates at the top sur- face of the Ag(111) thin film, which favors 2D germanene islanding at about 200 °C, the temperature where we per- formed the simultaneous deposition of 0.3 monolayers of Sn. By this procedure we obtained remarkably precise ger- manene/stanene heterojunctions without significant replace- ment of Ge atoms in stanene and vice versa. In experiments, the atomic and electronic structures have been determined by low-energy electron diffraction (LEED), scanning tun- neling microscopy (STM), and scanning tunneling spectros- copy (STS).

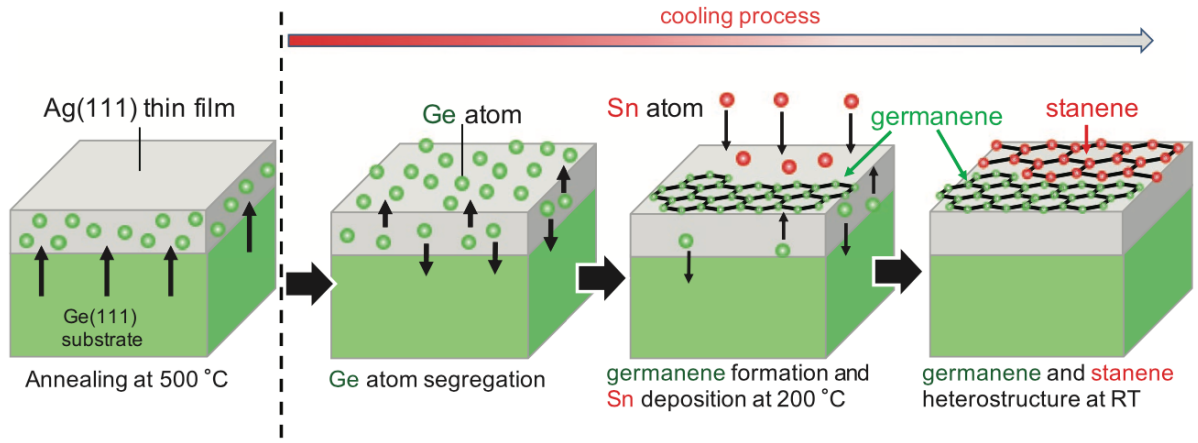

Figure 1. Illustration of the sequential formation of lateral heterostructures of germanene and stanene, prepared on a Ag(111) thin film grown on a Ge(111) substrate after annealing at 500 °C, followed by slow cooling. A Sn deposition is performed at 200 °C during the Ge segregation and germanene formation processes while cooling, resulting in the growth of lateral heterostructures of germanene and stanene observed at room temperature.

2. Results and Discussion

Figure 2a displays the LEED pattern for a stanene sheet formed at 200 °C by MBE over a Ag_2Sn initial surface alloy grown on a Ag(111) single crystal, in conditions sim- ilar to those used in our previous work on the synthesis of stanene.[26] It shows the primitive spots of epitaxial stanene with a unit cell 0.50 nm in size (see Figure 2e), corresponding to a Ag(111)($\sqrt{3} \times \sqrt{3}$)R30° super periodicity. The corresponding STM image, revealing the honeycomb atomic arrangement of epitaxial monolayer stanene having a 0.50 nm unit cell, in perfect match with the underlying Ag_2Sn surface alloy with ($\sqrt{3} \times \sqrt{3}$)R30° superstructure with respect to Ag(111), is displayed in Figure 2b. Figure 2c shows the LEED pattern for a complete germanene sheet formed also at 200 °C on top of a Ag(111) thin film previously grown on Ge(111) upon segregation of germanium during slow cooling, after initial heating of the specimen at 500 °C. The primitive spots originating from the honeycomb lattice of germanene, which correspond to Ag(111)"1.35 × 1.35"R30° with 0.39 nm size (see Figure 2e), are clearly observed. Additional spots originate from the prominent characteristic 2D ($3\sqrt{21} \times 3\sqrt{21}$) R10.9° germanene superstructure observed in STM imaging (shown in Figure 2d), matching a Ag(111)($7\sqrt{7} \times 7\sqrt{7}$)R19° superstructure. Here, we emphasize that these LEED pat- terns and STM images are in perfect accordance with those obtained in previous papers.[24,26]

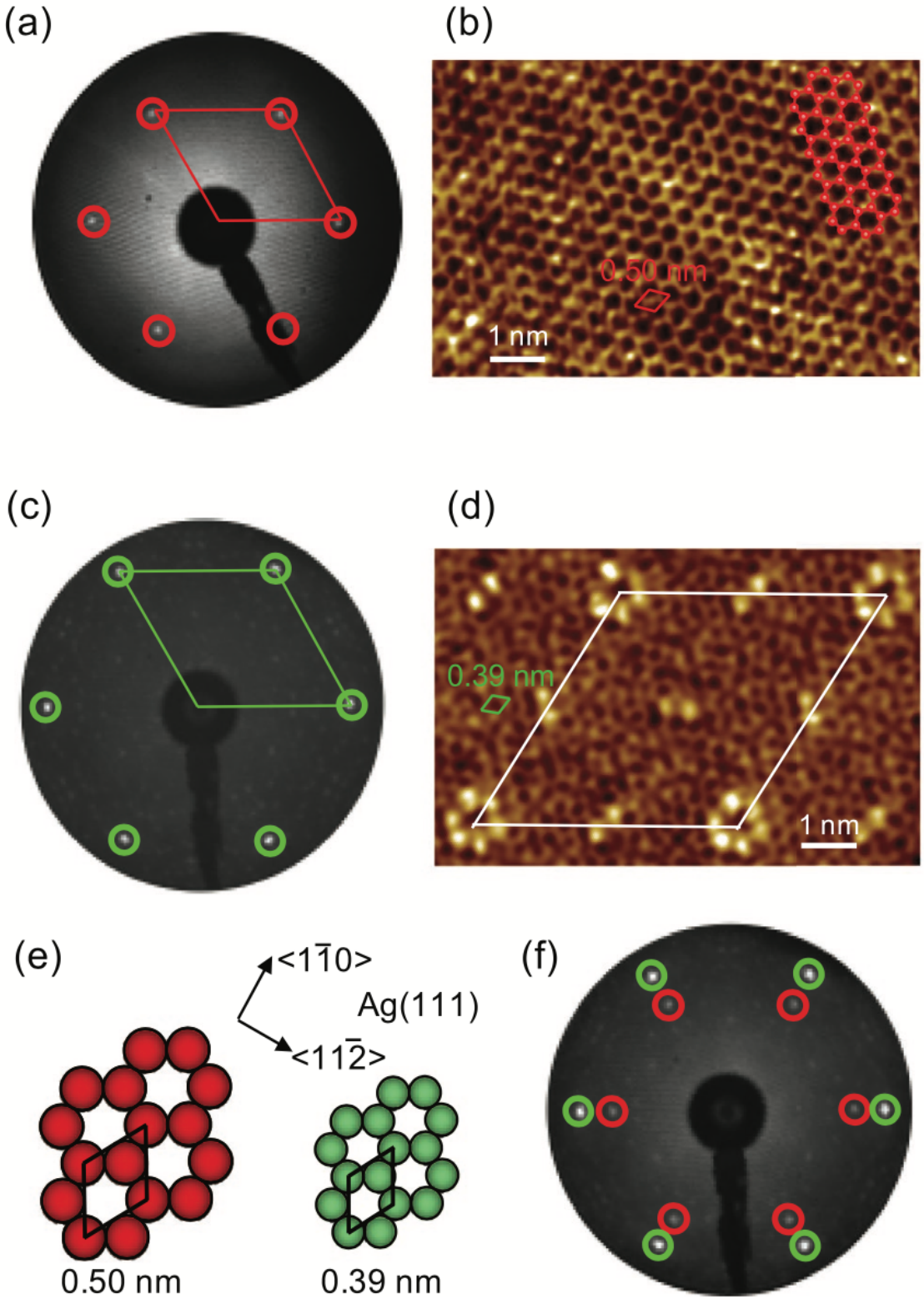

Figure 2. LEED patterns at 36 eV incident electron energy and STM images of a–b) stanene grown by deposition on a Ag_2Sn surface alloy and c–d) germanene grown by segregation on a Ag(111) thin film in epi- taxy on a Ge(111) substrate. e) Ball models of the oriented stanene and germanene sheets. f) LEED pattern at 36 eV incident electron energy of the lateral heterostructures of germanene and stanene grown in synergy on a Ag(111) thin film in epitaxy on a Ge(111) substrate.

For direct comparison, Figure 2f shows the LEED pattern for the heterostructure built up on a Ag(111) thin film grown on a Ge(111) substrate, following the recipe described above. No other spots, besides those in Figure 2a,c are seen, which indi- cates that no ordered new structure composed of intermixed Sn and Ge atoms is formed. Furthermore, within the resolu- tion limits, the positions of the LEED spots are identical to a superposition of those stemming from the sole germanene and stanene overlayers, shown in Figure 2a,c. It indicates that pure germanene and stanene domains are obtained by our methodology, which may possibly point to the realization of lateral heterojunctions.

Actually, this is effectively confirmed in STM micro- scopy observations. **Figure 3**a shows the STM image corre- sponding to the LEED pattern shown in Figure 2f. On the (111) terraces of the silver thin film, the characteristic 2D ($3\sqrt{21} \times 3\sqrt{21}$)R10.9° germanene superstructure, matching a Ag(111)($7\sqrt{7} \times 7\sqrt{7}$)R19° superperiodicity,[24] is easily recog- nized upon comparison with Figure 2d. It surrounds, two rounded 2D islands, with diameters of several tens nm. One is observed on a single terrace, while the other one carpets the straight step. From the section profile along A-B, the height difference of the two successive germanene covered terraces is 0.23 nm (Figure 3b), corresponding to the mono- atomic step height of Ag(111). The embedded island is only 0.04 nm higher than the surrounding germanene covered terrace, as determined from the C-D section profile shown in Figure 3c. This is just the difference between the Sn and Ge atomic diameters. We stress that no 3D islands are observed in the wide-scale STM images. Furthermore, as the areal ratio of the observed stanene islands is rather smaller than the one which could be expected for the Sn 0.3 monolayer (ML) deposition, therefore, some Sn atoms might have con- currently dissolved into the Ag(111) thin film.

A zoom-in at atomic-scale of the STM image of the island shown in Figure 3d (red square in Figure 3a) reveals the clear honeycomb structure of epitaxial stanene, matching a Ag(111) ($\sqrt{3} \times \sqrt{3}$)R30° superstructure initially formed by a Ag_2Sn sur- face alloy underneath, as discussed above, and precisely char- acterized earlier.[26] The honeycomb structure appears highly perfect, exhibiting no specific distortion, defects or protrusions that could have originated from substituted or on-top Ge atoms. It means that monolayer stanene is prepared without any replacement or adsorption of Ge atoms.

Similarly, a zoom-in at atomic-scale of the surrounding germanene area (Figure 3e) reveals the specific features, namely hexagons and double protrusions constitutive of the 2D ($3\sqrt{21} \times 3\sqrt{21}$)R10.9° germanene superstructure, which char- acterize the STM images of the perfectly oriented germanene sheet formed by germanium segregation and ordered assembly on the silver thin film initially grown on Ge(111),[24] as already displayed in Figure 2d.

We now underline that if instead of the pure Ag(111) tem- plate, the Ag_2Sn surface alloy with ($\sqrt{3} \times \sqrt{3}$)R30° periodicity with respect to Ag(111)1 × 1 was lying beneath the germanene sheet, the ($7\sqrt{7} \times 7\sqrt{7}$)R19° superstructure with respect to silver (111) could not have formed, because of the crystallographic incompatibility between ($7\sqrt{7} \times 7\sqrt{7}$)R19° and ($\sqrt{3} \times \sqrt{3}$)R30° super periodicities.

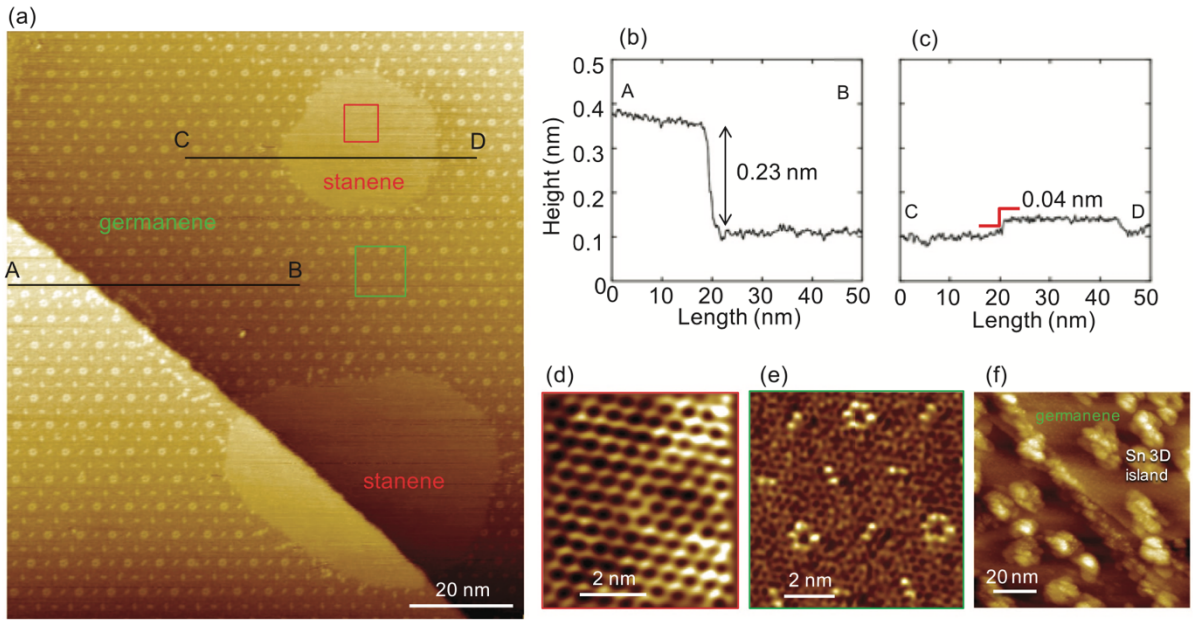

Figure 3. Lateral heterostructures of germanene and stanene observed at RT. They were prepared on a Ag(111) thin film grown on a Ge(111) substrate after annealing at the substrate temperature of 500 °C. During the cooling process, where Ge segregation takes place, a Sn deposition of 0.3 ML at 200 °C was performed. a) Large-scale STM image (U_S = +1.5 V, I = 200 pA). b) Section profile along the A-B black line in (a). c) Section profile along the C-D black line in (a). d) Atomic-scale STM image of the embedded stanene island within the red square in (a) (U_S = +0.4 V, I = 200 pA). e) Atomic- scale STM image of the surrounding germanene sheet within the green square in (a) (U_S = +1.0 V, I = 200 pA). f) Wide-scale STM image prepared on a Ag(111) thin film grown on a Ge(111) substrate after annealing at the substrate temperature of 500 °C with a Sn deposition of 0.3 ML at 150 °C during the cooling process. (U_S = +1.5 V, I = 200 pA), showing Sn 3D islanding at this too low temperature.

When the temperature chosen for Sn deposition during the cooling process of the Ag(111) thin film on the Ge(111) substrate is higher than about 220 °C, for example 260 °C, the surface is completely covered by germanene and no stanene phase is observed: the STM images look like the one shown in Figure 2d. Furthermore, as no 3D Sn islands appear, all deposited Sn atoms have dissolved into the silver film.

At variance, as shown above in Figure 3a, Sn atoms form large atom-thin 2D stanene islands upon deposition at 200 °C.

We note that most often more or less rounded stanene islands are formed, although elongated ones are also present. This points to rather isotropic on-surface diffusion processes, as well as similar lateral growth velocities along the main crystal- lographic directions, consequently indicating not markedly dif- ferent edge energies.

Now, if instead, the deposition temperature chosen during the cooling process is too low, for example, 150 °C or less, on the contrary, 3D Sn islands are formed over the germanene sheet, as shown in Figure 3f. These results indicate that once a full germanene sheet overlays the

Ag(111) surface, Sn atoms cannot kick away Ge atoms from germanene; instead, they just form 3D Sn islands on top of the germanene overlayer.

Hence, if Sn is deposited before the germanene sheet fully covers the entire surface upon cooling the substrate, Sn atoms can form stanene and/or a Ag_2Sn surface alloy on the remaining bare areas. In other words, the heterostructures can be realized only in a narrow temperature window because of the competitive, kinetically driven processes, namely, on the one hand, Ge atom diffusion through the thin Ag(111) film, segregation on top, and surface diffusion to permit 2D germanene nucleation and lateral spreading, and, on the other hand, enough Sn atoms diffusing on the surface to nucleate 2D stanene islands on areas not yet covered by germanene. Said differently, if the Sn deposition temperature is too high, tin dissolves into the Ag thin film, if it is too low, a complete ger- manene overlayer has enough time to form, on top of which tin cannot form a stanene wetting layer, which results in 3D growth. Hence, the temperature chosen for the deposition of tin plays a crucial role.

A close-up STM image of the stanene island of Figure 3a, is shown in **Figure 4**a to examine the boundaries of the ger- manene and stanene domains of the lateral heterostructures. Red solid lines indicate some preferential directions for the domain boundaries. They are 30° clock-wise rotated toward the Ag(111) <112> direction, which is the germanene zig-zag direction, and 19° anti-clock-wise rotated from a unit vector of the Ag(111)($7\sqrt{7} \times 7\sqrt{7}$)R19° superstructure. Figure 4b displays the boundary region between stanene and germanene (for a different preparation) at atomic resolution. Although it is dif- ficult to image both sides in the same tunneling conditions, one clearly recognizes a zig-zag edge for the stanene island on the left side, and the fingerprint protrusions of the germanene sheet on the right side, also pointing to a zig-zag termination. If not truly atomically perfect, as one could desire, neverthe- less, the interface appears very narrow, with minimal disorder, pointing to a fairly abrupt junction.

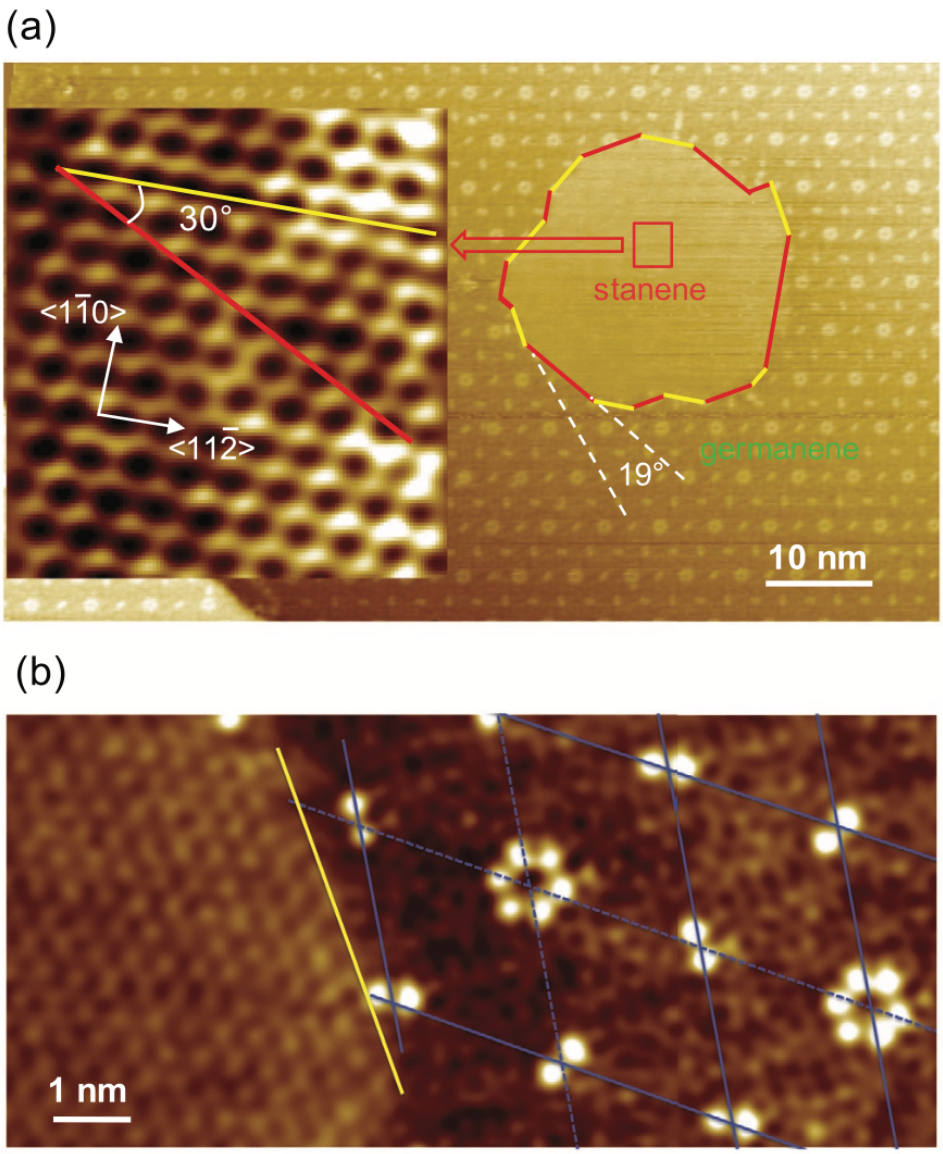

Figure 4. a) STM image of the lateral in-plane heterostructure of stanene and germanene (U_S = +1.5 V, I = 200 pA). The solid yellow and red lines represent domain boundaries with zigzag and armchair edges. b) High- resolution STM image of a zig-zag boundary of the lateral in-plane hetero- structure of germanene and stanene (U_S = +1.5 V, I = 200 pA).

A schematic illustration of perfect zig-zag and armchair junc- tions between germanene and stanene on Ag(111) is displayed in **Figure 5**. The unit cells of the honeycomb structures of ger- manene and stanene with sides 1.35a_{Ag} and $\sqrt{3}a_{Ag}$ along the Ag<112> and equivalent directions are rotated by 30° from that of Ag(111), whose a_{Ag} sides are along the Ag<110> and equiva- lent directions.

From the STM image of Figure 4a, the domain boundary of germanene is rotated by 19° toward the anti-clock-wise direction from the Ag(111)($7\sqrt{7} \times 7\sqrt{7}$)R19° superstructures; a germanene armchair edge is thus formed. The STM images also indicate that the domain boundaries for stanene are rotated 30° toward the clock-wise direction from the Ag(111)($\sqrt{3} \times \sqrt{3}$)R30° super-structures. Hence, a stanene armchair edge is also formed. Therefore, the domain boundary,

which is along the Ag(111) <1-10> direction, has armchair edges for both domains. Because the orientations of the honeycomb structures of germanene and stanene are identical to each other, the domain boundary has the same edge structure, but with different atom spacings. We notice that most domain boundaries share armchair edges, signaling minimum energy equilibrium configuration, but zigzag edges are also observed in the STM images, as shown in Figure 4b.

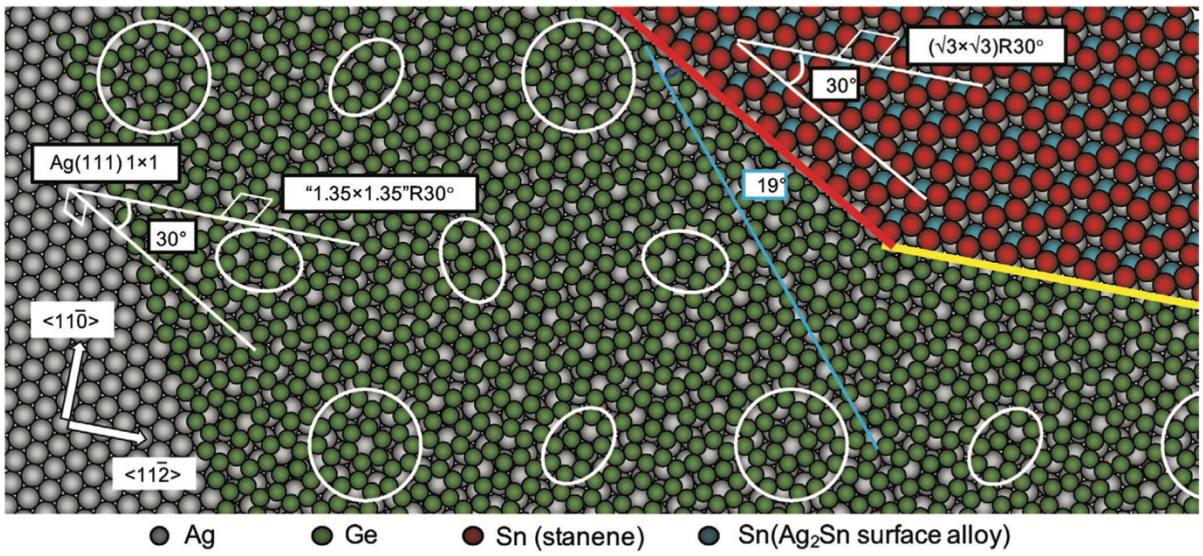

Figure 5. Structural model of the lateral heterostructure of germanene and stanene on Ag(111) with armchair (marked by a red line) and zig-zag (marked by a yellow line), keeping the unit cell of germanene and stanene, namely, 1.35 × 1.35R30° and (√3 × √3)R30°, respectively. The areal positions corresponding to the hexagonal and double-dotted protrusions in Figure 3e are marked by white circles and ovals.

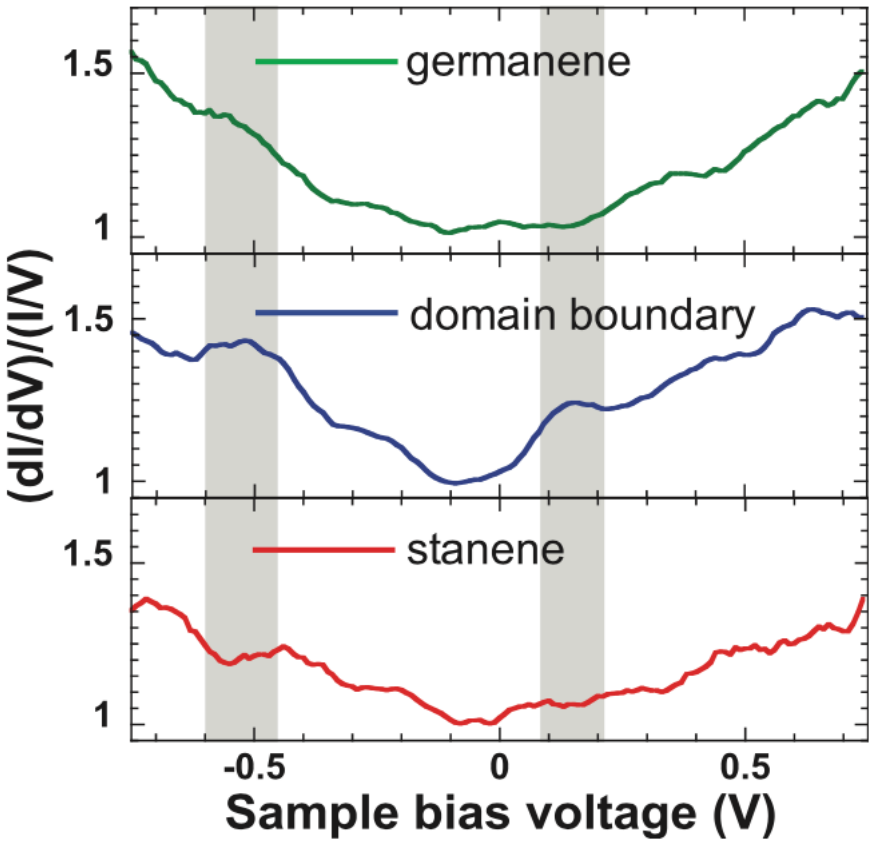

Figure 6. STS spectra of a germanene zone, a zigzag domain boundary region, and a stanene zone of the heterostructure on the same terrace of the Ag(111) thin film.

Figure 6 shows (d*I*/d*V*)/(*I*/*V*) STS spectra for the lateral het- erostructure of stanene embedded in germanene recorded on the germanene and stanene domains, and over a region span- ning a zig-zag domain boundary. Clearly two characteristic peaks emerge at the domain boundary at –0.5 and +0.15 eV sample biases. We relate these features to a characteristic elec- tron density of states for filled and empty edge states.

The fabrication of the first silicene transistor operating at RT in 2015[30] has opened exciting prospects for future 2D electronics.[33,34] Compatible with the current Si-based tech- nology, germanene and stanene, which are 2D topological insu- lators with significantly stronger spin-orbit couplings[31] are highly promising new contenders.[34] The realization of a lateral in-plane heterostructure between germanene and embedded stanene nanodots is unprecedented. To the best of our knowl- edge, until now, such heterostructures have been obtained, on the one hand, only between graphene and h-BN since 2012[32–34] and with transition metal dichalcogenides since 2014, on the other hand.[8] These novel heterostructures will further boost fundamental studies, not only in electronics, but also, typically, in spintronics and optoelectronics.[37] Progress in engineering, for example, to tailor nanoribbons and lateral superlattices, and use such effects as negative differential resistance, can be [35–38] anticipated. Recently, multilayers of germanene, stanene, and antimonene have been grown directly on semiconducting molybdenum disulfides;[39] indeed, an exciting prospect would be the lateral growth of heterostructures between them.

To summarize, revolutionary developments can be foreseen, none the least in quantum science, but also for new tantalizing functional nano-devices.

3. Conclusion

We have successfully prepared at the nanoscale nearly atomi- cally precise lateral monolayer heterostructures of stanene embedded in germanene on a silver (111) thin film epitaxially grown on a Ge(111) substrate thanks to a synergetic combina- tion of germanium segregation from the Ge(111) substrate and tin deposition from a Sn evaporation source. The combined STM and LEED observations testify that the lateral structures on either side of the heterojunctions are pure germanene and pure stanene monolayers, respectively. The domain boundaries have mostly armchair edges, but zigzag edges are also formed. From the STS spectra, 1D edge states are revealed. To the best of our knowledge this is the first realization of a lateral hetero- junction between group 14 elemental post-graphene 2D mate- rials, whose outstanding electronic properties open exciting prospects for disruptive technologies, such as the future fabri- cation of functional 2D nano-devices compatible with conven- tional Si-based technology.

4. Experimental Section

The experiments were performed using an ultrahigh-vacuum (UHV) system at Nagoya University. The system consisted of a preparation chamber with a base pressure below 5×10^{-10} mbar, and an analysis chamber with a base pressure below 10^{-10} mbar.

Silver thin films (100 nm thick) were prepared on a Ge(111) substrate by conventional thermal evaporation. The details of the sample preparation of Ag thin films on Ge(111) and segregation phenomena of the Ge atoms by subsequent annealing under N_2 atmosphere are described in previous reports.[40–42] Clean Ag(111) surfaces were prepared by 2 keV Ar^+ ion sputtering at RT, followed by annealing the sample at the temperature of 400 °C. Annealing was performed by electron bombardment of the sample holder at an emission current of 5 mA and a voltage of –650 V. The sample temperature was monitored with a radiation thermometer and a type K thermocouple mounted on the base plate of the sample holder. The cleanliness of the surface was measured by Auger electron spectroscopy after sputtering and annealing; no contaminants, such as C and O, were observed within the detection limits, and a sharp (1 × 1) LEED pattern was observed.

After annealing the sample at 500 °C, tin was deposited onto the Ag(111) surface during the cooling process at various temperatures from 300 °C down to RT in UHV from a well degassed quartz crucible evaporator operating at a deposition rate of approximately 0.1 ML min^{-1}, as measured by placing a quartz crystal microbalance at the sample position. 1 ML was defined as a Sn overlayer with the atomic density of a Ag(111) plane: 1.38×10^{15} atoms cm^{-2}. The deposition rate was accurately calibrated in advance by Rutherford backscattering spectroscopy (RBS). For the RBS measurement, a graphite substrate with an ultra-thin tin film on the surface was prepared. Details of the experimental setup for RBS have been published elsewhere.[43,44] The amounts of deposited tin were about 0.3 ML; errors in mentioned coverage ratios were less than 5%.

The system was equipped with a rear-view LEED system operating with a LaB_6 filament and a UHV STM system (Omicron STM-1). All STM images presented were acquired at RT with W tips, electrochemically etched in a KOH solution, in a constant current mode. All apparatuses were situated on an air damper with an active vibration isolation system (Kurashiki). STS

spectra were obtained together with the simultaneous STM measurements by numerical derivative of tunneling current (I) versus sample bias voltage (V) and averaging over 20 equivalent sites to reduce noise.

Acknowledgements

J.Y. acknowledges financial support from Toyoaki Scholarship Foundation and the Murata Science Foundation in 2017 and 2019, respectively. G.L.L. acknowledges support from Nagoya University thanks to two “Eminent Foreign Scientist” Invitation Awards in 2015–2016 and in 2019–2020, as well as an Invitational Fellowship for Research in Japan by the Japan Society for the Promotion of Science (JSPS) in 2017.

References

[1] P. Vogt, P. de Padova, C. Quaresima, J. Avila, E. Frantzeskakis, M. C. Asensio, A. Resta, B. Ealet, G. Le Lay, *Phys. Rev. Lett.* **2012**, *108*, 155501.

[2] A. Fleurence, R. Friedlein, T. Ozaki, H. Kawai, Y. Wang, Y. Yamada-Takamura, Phys. Rev. Lett. 2012, 108, 245501.

[3] M. E. Dávila, L. Xian, S. Cahangirov, A. Rubio, G. Le Lay, New J. Phys. 2014, 16, 095002.

[4] F. Zhu, W. Chen, Y. Xu, C. Gao, D. Guan, C. Liu, D. Qian, S.-C. Zhang, J. Jia, Nat. Mater. 2015, 14, 1020.

[5] J. Yuhara, B. He, N. Matsunami, M. Nakatake, G. Le Lay, Adv. Mater. 2019, 31, 1901017.

[6] L. Liu, J. Park, D. A. Siegel, K. F. McCarty, K. W. Clark, W. Deng, L. Basile, J. C. Idrobo, A.-P. Li, G. Gu, Science 2014, 343, 163.

[7] J. Li, V. B. Shenoy, Appl. Phys. Lett. 2011, 98, 013105.

[8] J. Zhao, K. Cheng, N. Han, J. Zhang, Wiley Interdiscip. Rev.: Comput. Mol. Sci. 2018, 8, e1353.

[9] X. Liu, M. C. Hersam, Sci. Adv. 2019, 5, eaax6444.

[10] X.-S. Ye, Z.-G. Shao, H. Zhao, L. Yang, C.-L. Wang, RSC Adv. 2014, 4, 21216.

[11] L. Matthes, O. Pulci, F. Bechstedt, J. Phys.: Condens. Matter 2013, 25, 395305.

[12] A. Debernardi, L. Marchetti, Phys. Rev. B 2016, 93, 245426.

[13] S. Kaneko, H. Tsuchiya, Y. Kamakura, N. Mori, M. Ogawa, Appl.

Phys. Express 2014, 7, 035102.

[14] L. Meng, Y. Wang, L. Zhang, S. Du, R. Wu, L. Li, Y. Zhang, G. Li,

H. Zhou, W. A. Hofer, H.-J. Gao, Nano Lett. 2013, 13, 685.

[15] L. Li, S. Lu, J. Pan, Z. Qin, Y. Wang, Y. Wang, G. Cao, S. Du,

H.-J. Gao, Adv. Mater. 2014, 26, 4820.

[16] M. Derivaz, D. Dentel, R. Stephan, M.-C. Hanf, A. Mehdaoui,

P. Sonnet, C. Pirri, Nano Lett. 2015, 15, 2510.

[17] J. Gou, Q. Zhong, S. Sheng, W. Li, P. Cheng, H. Li, L. Chen, K. Wu,

2D Mater. 2016, 3, 045005.

[18] Z. Qin, J. Pan, S. Lu, Y. Shao, Y. Wang, S. Du, H.-J. Gao, G. Cao,

Adv. Mater. 2017, 29, 1606046.

[19] C.-H. Lin, A. Huang, W. W. Pai, W.-C. Chen, T.-Y. Chen, T.-R. Chang,

R. Yukawa, C.-M. Cheng, C.-Y. Mou, I. Matsuda, T.-C. Chiang,

H.-T. Jeng, S.-J. Tang, Phys. Rev. Mater. 2018, 2, 024003.

[20] P. Bampoulis, L. Zhang, A. Safaei, R. van Gastel, B. Poelsema,

H. J. W. Zandvliet, J. Phys.: Condens. Matter 2014, 26, 442001.

[21] L. Zhang, P. Bampoulis, A. N. Rudenko, Q. Yao, A. van Houselt, B. Poelsema, M. I. Katsnelson, H. J. W. Zandvliet, Phys. Rev. Lett.

2016, 116, 256804.

[22] L. Persichetti, F. Jardali, H. Vach, A. Sgarlata, I. Berbezier,

M. De Crescenzi, A. Balzarotti, J. Phys. Chem. Lett. 2016, 7, 3246.

[23] J. Zhuang, C. Liu, Z. Zhou, G. Casillas, H. Feng, X. Xu, J. Wang, W. Hao, X. Wang, S. X. Dou, Z. Hu, Y. Du, Adv. Sci. 2018, 5, 1800207.

[24] J. Yuhara, H. Shimazu, K. Ito, A. Ohta, M. Araidai, M. Kurosawa, M. Nakatake, G. Le Lay, ACS Nano 2018, 12, 11632.

[25] J. Gou, L. Kong, H. Li, Q. Zhong, W. Li, P. Cheng, L. Chen, K. Wu, Phys. Rev. Mater. 2017, 1, 054004.

[26] J. Yuhara, Y. Fujii, K. Nishino, N. Isobe, M. Nakatake, L. Xian, A. Rubio, G. Le Lay, 2D Mater. 2018, 5, 025002.

[27] J. Deng, B. Xia, X. Ma, H. Chen, H. Shan, X. Zhai, B. Li, A. Zhao, Y. Xu, W. Duan, S.-C. Zhang, B. Wang, J. G. Hou, Nat. Mater. 2018, 17, 1081.

[28] R. W. Olesinski, G. J. Abbaschian, J. Alloy Phase Diagrams 1984, 5, 265. [29] R. W. Olesinski, G. J. Abbaschian, J. Alloy Phase Diagrams 1984,

5, 180.

[30] L. Tao, E. Cinquanta, D. Chiappe, C. Grazianetti, M. Fanciulli,

M. Dubey, A. Molle, D. Akinwande, Nat. Nanotechnol. 2015,

10, 227.

[31] M. Kurpas, P. E. Faria Junior, M. Gmitra, J. Fabian, Phys. Rev. B 2019,

100, 125422.

[32] T. H. Nguyen, D. Perilli, M. Cattelan, H. Liu, F. Sedona, N. A. Fox,

C. di Valentin, S. Agnoli, Nano Res. 2019, 12, 675.

[33] P. Zhuang, W. Lin, H. Chou, A. Roy, W. Cai, S. K. Banerjee, Nano-

technology 2019, 30, 03LT01.

[34] Q. Wu, W. Wongwiriyapan, J.-H. Park, S. Park, S. J. Jung, T. Jeong,

S. Lee, Y. H. Lee, Y. J. Song, Curr. Appl. Phys. 2016, 16, 1175.

[35] J. Wang, Z. Li, H. Chen, G. Deng, X. Niu, Nano-Micro Lett. 2019,

11, 48.

[36] Y. An, M. Zhang, D. Wu, T. Wang, Z. Jiao, C. Xia, Z. Fu, K. Wang,

Phys. Chem. Chem. Phys. 2016, 18, 27976.

[37] M. Ge, C. Si, Carbon 2018, 136, 286.

[38] M. P. Levendorf, C.-J. Kim, L. Brown, P. Y. Huang, R. W. Havener,

D. A. Muller, J. Park, Nature 2012, 488, 627.

[39] K.-C. Chen, L.-M. Lee, H.-A. Chen, H. Sun, C.-L. Wu, H.-A. Chen,

K.-B. Lin, Y.-C. Tseng, C.-C. Kuan, C.-W. Pao, S.-Y. lin, Semicond. Sci.

Technol. 2019, 34, 105020.

[40] M. Kurosawa, A. Ohta, M. Araidai, S. Zaima, Jpn. J. Appl. Phys. 2016,

55, 08NB07.

[41] K. Ito, A. Ohta, M. Kurosawa, M. Araidai, M. Ikeda, K. Makihara, S. Miyazaki, Jpn. J. Appl. Phys. 2018, 57, 04FJ05.

[42] K. Ito, A. Ohta, M. Kurosawa, M. Araidai, M. Ikeda, K. Makihara, S. Miyazaki, Jpn. J. Appl. Phys. 2018, 57, 06HD08.

[43] J. Yuhara, M. Inoue, K. Morita, J. Vac. Sci. Technol., A 1992, 10, 334.

[44] J. Yuhara, K. Morita, J. Falta, B. H. Müller, M. H.-v. Hoegen, Surf. Interface Anal. 2001, 31, 754.